

# Effect of B<sub>2</sub>O<sub>3</sub> on Crystallization Behavior, Structure, and Heat Transfer of CaO-SiO<sub>2</sub>-B<sub>2</sub>O<sub>3</sub>-Na<sub>2</sub>O-TiO<sub>2</sub>-Al<sub>2</sub>O<sub>3</sub>-MgO-Li<sub>2</sub>O Mold Fluxes



JIAN YANG, JIANQIANG ZHANG, YASUSHI SASAKI, OLEG OSTROVSKI, CHEN ZHANG, DEXIANG CAI, and YOSHIAKI KASHIWAYA

The effect of B<sub>2</sub>O<sub>3</sub> on crystallization behavior, structure, and heat transfer of CaO-SiO<sub>2</sub>-Na<sub>2</sub>O-B<sub>2</sub>O<sub>3</sub>-TiO<sub>2</sub>-Al<sub>2</sub>O<sub>3</sub>-MgO-Li<sub>2</sub>O fluorine-free mold fluxes was investigated using hot thermocouple technique (HTT), Raman spectroscopy, and infrared emitter technique (IET), respectively. The critical cooling rate in continuous cooling experiments decreased and the incubation time determined in isothermal experiments increased with increasing B<sub>2</sub>O<sub>3</sub> content, both implying a decreasing crystallization tendency. The major phases of mold fluxes determined using X-ray diffraction changed from Ca<sub>2</sub>MgSi<sub>2</sub>O<sub>7</sub> and Ca<sub>11</sub>Si<sub>4</sub>B<sub>2</sub>O<sub>22</sub> to CaSiO<sub>3</sub> with the increasing amount of B<sub>2</sub>O<sub>3</sub>. B<sub>2</sub>O<sub>3</sub> increased the degree of polymerization in silicate network, forming 3D borate structures. Addition of B<sub>2</sub>O<sub>3</sub> decreased the flux melting temperature which has a significant impeding effect on the crystal nucleation and growth. The heat flux of mold fluxes measured using IET showed that the increase of B<sub>2</sub>O<sub>3</sub> from 4.7 to 6.8 mass pct impeded the heat flux; while a further increase of B<sub>2</sub>O<sub>3</sub> from 6.8 to 10.4 mass pct promoted the heat transfer. This phenomenon was attributed to the variation of crystallization behavior and crystal morphology with different B<sub>2</sub>O<sub>3</sub> content in the mold fluxes.

DOI: 10.1007/s11663-017-0997-6

© The Minerals, Metals & Materials Society and ASM International 2017

## I. INTRODUCTION

MOLD fluxes are indispensable for the continuous casting of defect-free steel products, providing appropriate heat transfer control, lubrication, thermal insulation, inclusion entrapment, and oxidation prevention.<sup>[1]</sup> The amount of heat withdrawn from liquid steel during solidification is primarily dependent upon the thermo-physical properties of mold flux film. An inappropriate control of heat transfer in continuous casting process could result in a breakout of steel strand and even a halt of operation if heat transfer rate is excessively low, or longitudinal cracks caused by uneven heat distribution along solidifying steel strand surface if the heat transfer rate is too high.<sup>[2,3]</sup> Therefore,

understanding the heat transfer phenomenon between steel strand and copper mold is important for the prevention of the aforementioned imperfections. Mold fluxes with high crystallization tendency are typically recommended in the casting of cracking-sensitive steel. The thick crystalline layer is effective in suppressing heat removal from liquid steel in terms of its high thermal resistance. The grain boundaries of crystals scatter photons, which reduces radiative heat transfer.<sup>[4,5]</sup> Pores, cracks formed in the crystalline layer, and air gaps between the mold and the flux film also exert a high thermal resistance, which minimizes the unevenness of steel shell and, therefore, the localized thermal stresses on a solidified shell.<sup>[4-6]</sup> Currently, most of the commercial mold fluxes contain fluorides, *e.g.*, CaF<sub>2</sub> and NaF, to control heat transfer rate through the precipitation of cuspidine; fluorides also decrease the viscosity of mold fluxes.<sup>[7-9]</sup> However, the emission of gaseous fluorides, such as HF, SiF<sub>4</sub>, and NaF, at high temperature brings about dreadful pollution to atmosphere (acid rain), ground water (low pH-value), and health problems (brain, bone, kidney damages, *etc.*).<sup>[1,10-17]</sup> Taking account of the ever-rising environmental concern for steelmaking industry, the development of fluorine-free mold fluxes is of great significance. The major challenge in the development of fluorine-free mold fluxes is an effective control of heat transfer.

---

JIAN YANG, JIANQIANG ZHANG, YASUSHI SASAKI, and OLEG OSTROVSKI are with the School of Materials Science and Engineering, University of New South Wales, Sydney, NSW, 2052, Australia. Contact e-mail: j.q.zhang@unsw.edu.au CHEN ZHANG and DEXIANG CAI are with the Baosteel Group Corporation Research Institute, Shanghai, 201900, China. YOSHIAKI KASHIWAYA is with the Department of Energy Science and Technology, Kyoto University, Yoshida Honmachi, Sakyo-ku, Kyoto, 606-8501, Japan.

Manuscript submitted October 13, 2016.

Article published online May 18, 2017.

Although several substitutes for cuspidine were proposed in the fluorine-free mold fluxes, such as  $\text{Ca}_{11}\text{Si}_4\text{B}_2\text{O}_{22}$ ,<sup>[13–18]</sup>  $\text{Ca}_2\text{Si}_3\text{Na}_2\text{O}_9$ ,<sup>[11]</sup> and  $\text{CaSiTiO}_5$ ,<sup>[12]</sup> the lack of fundamental knowledge of crystallization of fluorine-free flux system inhibits their application in the steelmaking industry.  $\text{Ca}_{11}\text{Si}_4\text{B}_2\text{O}_{22}$  has recently been reported as a promising substitute for cuspidine with respect to its crystallization behavior and heat transfer ability.<sup>[13–17]</sup> It also has a similar melting point to cuspidine.<sup>[19,20]</sup> Therefore, understanding the precipitation behavior of  $\text{Ca}_{11}\text{Si}_4\text{B}_2\text{O}_{22}$  is important to the development of fluorine-free mold fluxes.

$\text{B}_2\text{O}_3$  is an important component for mold flux design as a flux agent. It becomes more appealing for the design of fluorine-free mold fluxes as the addition of  $\text{B}_2\text{O}_3$  lowers the viscosity and the melting temperature of mold fluxes, which may replicate the role of fluorides in terms of lubrication.<sup>[13,21–25]</sup> The effects of  $\text{B}_2\text{O}_3$  on the crystallization and heat transfer of low-fluorine mold fluxes have been reported.<sup>[26,27]</sup> However, there are few investigations on the fluoride-free mold fluxes, and the mechanism of  $\text{B}_2\text{O}_3$  affecting crystallization behavior is yet to be clarified. The variable structure of borate groups in borosilicate mold fluxes makes their solidification behavior rather complicated.  $\text{B}_2\text{O}_3$  is normally considered as a network former; it can be incorporated into the silicate network resulting in a borosilicate structure with even higher structural complexity, which should restrain the crystallization tendency of mold fluxes.<sup>[1,13,21–23]</sup> However, it is also reported that the addition of  $\text{B}_2\text{O}_3$  reduces viscosity of mold fluxes,<sup>[1,13,22–25]</sup> which should benefit crystallization process by increasing the diffusion kinetics for nucleation and crystal growth. The heat transfer rate of mold fluxes is also affected by the addition of  $\text{B}_2\text{O}_3$  as a considerable portion of glass may form during solidification.<sup>[23]</sup> Moreover,  $\text{B}_2\text{O}_3$  is an essential constituent to form  $\text{Ca}_{11}\text{Si}_4\text{B}_2\text{O}_{22}$ , which is proposed to substitute cuspidine in the design of fluorine-free mold fluxes. The aim of this work is to investigate the effect of  $\text{B}_2\text{O}_3$  addition on the in-mold performance and structure of fluorine-free mold fluxes. The crystallization behavior, structure, and heat transfer of  $\text{CaO-SiO}_2\text{-B}_2\text{O}_3\text{-Na}_2\text{O-TiO}_2\text{-Al}_2\text{O}_3\text{-MgO-Li}_2\text{O}$  fluorine-free mold fluxes with different  $\text{B}_2\text{O}_3$  concentration were studied using hot thermocouple technique (HTT), Raman spectroscopy, and infrared emitter technique (IET), respectively.

## II. EXPERIMENTAL METHODS

### A. Sample Preparation

Compositions of the fluorine-free mold fluxes were designed on the basis of the thermodynamic modeling using FactSage as described elsewhere.<sup>[28]</sup> The pre-mixed reagent grade  $\text{CaCO}_3$ ,  $\text{SiO}_2$ ,  $\text{Al}_2\text{O}_3$ ,  $\text{B}_2\text{O}_3$ ,  $\text{Na}_2\text{CO}_3$ ,  $\text{TiO}_2$ ,  $\text{MgO}$ , and  $\text{Li}_2\text{CO}_3$  were melted at 1673 K (1400 °C) for 20 minutes in graphite crucibles.  $\text{CaCO}_3$ ,  $\text{Na}_2\text{CO}_3$ , and  $\text{Li}_2\text{CO}_3$  decomposed at high temperature, forming  $\text{CaO}$ ,  $\text{Na}_2\text{O}$ , and  $\text{Li}_2\text{O}$ , respectively. The melted fluxes were quenched onto a copper plate and then ground into

powders. Chemical compositions of the amorphous fluorine-free fluxes are listed in Table I, marked as Samples 1 to 4. The designed concentrations of  $\text{B}_2\text{O}_3$  in Samples 1 to 4 were 5, 7, 9, and 11 mass pct, respectively, but small  $\text{B}_2\text{O}_3$  loss was found. The concentrations of  $\text{B}_2\text{O}_3$  and  $\text{Li}_2\text{O}$  were determined by inductively coupled plasma (ICP) analysis, and other components were analyzed by X-ray fluorescence (XRF). Hemisphere temperature,  $T_{\text{hem}}$ , measured using a hot stage microscope, was also listed in Table I to reflect the melting properties of mold fluxes. The hemisphere temperature was defined as the temperature where the height of a flux powder cylinder decreases to 50 pct of its original height during a continuous heating process. The details of the measurement are described elsewhere.<sup>[29]</sup>

### B. Experimental Apparatus

#### 1. Hot thermocouple technique

The crystallization behavior of mold fluxes was determined by single hot thermocouple technique (SHTT) and double hot thermocouple technique (DHTT) (Professional Engineer Office KONNO, Japan).<sup>[30,31]</sup> The schematic setup of SHTT/DHTT is given in Figure 1(a). A hot thermocouple controls and measures the temperature simultaneously. Due to the low thermal inertia of the system, SHTT/DHTT could enable a high cooling rate up to 220 K/s by manual control or 30 K/s by automatic control, which makes it capable of simulating the highest cooling rate that mold fluxes encounter in the infiltration process.<sup>[31,32]</sup> The mold flux powders (*ca.* 10 mg) were mounted on a B-type thermocouple tip, and heated or cooled in accordance with the programmed temperature profile in SHTT; while the sample was attached between two thermocouples in DHTT, as shown in Figure 1(b). The crystallization process of mold fluxes was *in situ* observed and recorded by a video camera.

#### 2. Infrared emitter technique

The heat transfer across the flux disk was characterized by infrared emitter technique (IET) (Central South University, China).<sup>[23,33,34]</sup> The schematic layout of IET is given in Figure 2. Infrared radiation is emitted from a heating lamp with a set of tungsten filaments to the flux disk of standard size. The radiation intensity was adjusted by the applied voltage through a silicon controlled rectifier in accordance with a desired power profile. The wavelength of the radiation is close to that emitted from the solidifying steel strand.<sup>[23]</sup> A mold flux disk was placed on a copper base with four thermocouples embedded under the top surface of the copper base. The responding temperatures measured by the thermocouples at different depths were recorded and converted to the heat flux according to Fourier's law<sup>[33]</sup>:

$$q = \frac{-1}{n} \sum_i k \left( \frac{dT}{dx} \right)_i, \quad [1]$$

where  $q$  is the heat flux,  $n$  presents the total number of thermocouple pairs, and  $k$  refers to the thermal conductivity of copper.

**Table I. Chemical Compositions of Mold Fluxes with Different B<sub>2</sub>O<sub>3</sub> Concentration (Mass Pct)**

Sample	R	CaO	SiO <sub>2</sub>	Al <sub>2</sub> O <sub>3</sub>	B <sub>2</sub> O <sub>3</sub>	Na <sub>2</sub> O	TiO <sub>2</sub>	MgO	Li <sub>2</sub> O	T <sub>hem</sub> [K (°C)]
1	1.1	39.4	35.9	3.7	4.7	9.0	4.2	2.1	1.1	1325 (1052)
2	1.1	38.3	34.7	3.7	6.8	8.7	4.2	2.3	1.1	1297 (1024)
3	1.1	37.8	34.4	3.7	8.6	9.1	4.3	2.1	1.1	1257 (984)
4	1.1	36.9	33.3	3.7	10.4	8.4	4.4	2.1	1.1	1228 (955)

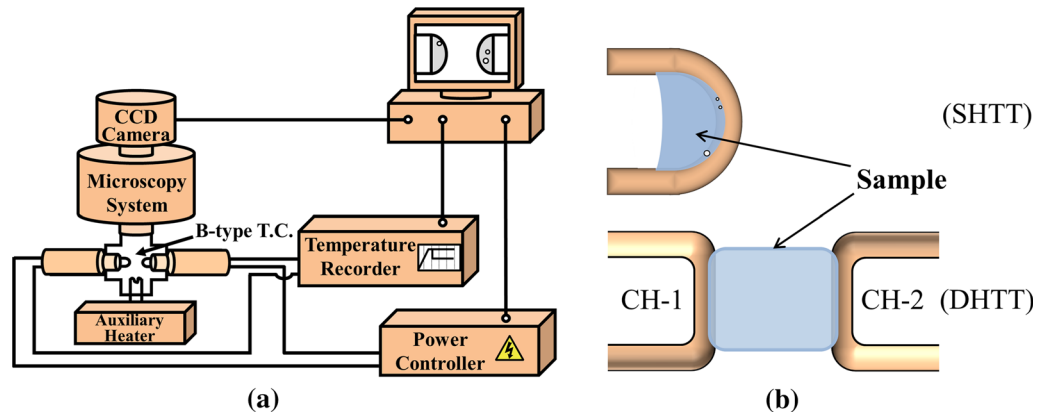


Fig. 1—Schematic representation of (a) hot thermocouple technique (HTT), (b) thermocouple setup.

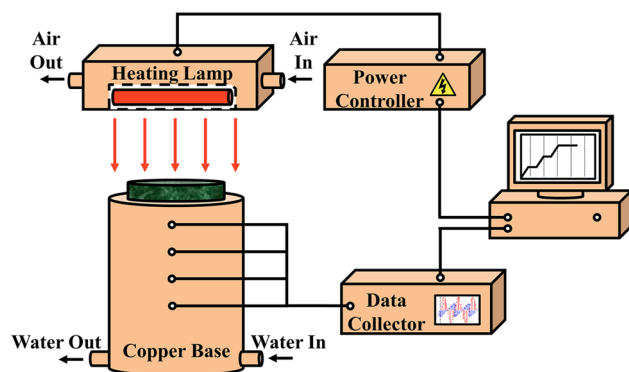


Fig. 2—Schematic representation of infrared emitter technique (IET).

### C. Experimental Procedures

#### 1. Crystallization behavior tests

Continuous cooling transformation (CCT) and time–temperature transformation (TTT) diagrams were constructed using SHTT in continuous cooling and isothermal experiments whose temperature profiles are given in Figures 3(a) and (b), respectively. In continuous cooling experiments, the sample was first heated to 1773 K (1500 °C), and held for 3 minutes to homogenize composition and remove bubbles. Then, it was continuously cooled down to 1073 K (800 °C) with different pre-set cooling ramps. The time and temperature at which the crystallinity of mold fluxes reached 0.5 vol pct were used to construct CCT curves. Three replicate measurements were conducted for the determination of crystallization temperatures at each cooling rate. It simulates the crystallization behavior in different cooling paths when molten fluxes infiltrate into the

interfacial gap between steel strand and copper mold.<sup>[30]</sup> Likewise, the sample was heated to 1773 K (1500 °C) in isothermal experiments and then rapidly quenched to different pre-set temperatures and held isothermally at the target temperatures until the crystallinity reached 100 vol pct. The times when crystallinity of mold fluxes reached 0.5 and 99 vol pct were defined as the onset and end of crystallization, respectively, which were used for the construction of TTT diagrams. Due to the influence of the power feedback, the cooling rate gradually dropped from 220 to 0 K/s within a few seconds when the real-time flux temperature was approaching the target temperature. Consequently, the starting point of isothermal treatment was defined as the time at which the tangent to the cooling path and the isothermal temperature line intersected.<sup>[16]</sup>

The precipitated phases in samples at different temperatures were analyzed using X-ray diffraction (XRD). Since the samples collected from the thermocouple tip were too tiny for the XRD analysis, 5 g amorphous samples were treated at 1173 K (900 °C) (low temperature zone) and 1273 K (1000 °C) (below the highest crystallization temperature of Sample 4), respectively, for 20 minutes in a furnace. The phase composition of the quenched samples was then identified using XRD (PANalytical X'pert Multipurpose X-ray Diffraction System, Netherlands) with Cu-K<sub>α</sub> radiation. The scan was conducted in the range of 2θ from 20 to 70 deg with a scanning speed of 0.021 deg/s.

Crystallization evolution of mold fluxes in a simulated thermal field was investigated in the DHTT experiments, of which the temperature profile is shown in Figure 3(c). A liquid flux film with a length of 1.5 mm was formed between two thermocouples when they were heated to 1773 K (1500 °C). High temperature thermocouple was

set at 1773 K (1500 °C) to simulate the temperature of liquid flux adjacent to the steel strand in meniscus zone,<sup>[35,36]</sup> while the low temperature thermocouple was pre-set to simulate the temperature of the cold surface of the flux film. Since the temperature of cold surface of flux film cannot be directly measured, it was calculated using Eq. [2] under one-dimensional heat transfer in the steady state<sup>[35,37,38]</sup>:

$$T_{CS} = T_M + q_T \cdot R_{INT}, \quad [2]$$

where  $T_{CS}$  is the temperature of cold surface of flux film,  $T_M$  is the temperature of hot surface of copper mold,  $q_T$  is the heat flux, and  $R_{INT}$  is the interfacial thermal resistance. According to the data acquired from the plant operation,  $T_M$  ranges from 423 K to 573 K (150 °C to 300 °C) which is consistent with the values reported in literatures.<sup>[35–37]</sup> The calculated average  $q_T$  is in the range of 0.75 to 2.05 MW/m<sup>2</sup> in plant operation for different steel grades and casting speeds, which accords with the reported values.<sup>[35–37,39]</sup> The value of  $R_{INT}$  was reported from  $0.83 \times 10^{-4}$  to  $8 \times 10^{-4}$  m<sup>2</sup> K/W.<sup>[35,37,39]</sup> In this study, the values of  $T_M$ ,  $q_T$ , and  $R_{INT}$  were assumed to be 473 K (200 °C), 1 MW/m<sup>2</sup>, and  $4 \times 10^{-4}$  m<sup>2</sup> K/W. Therefore, the calculated  $T_{CS}$  was 873 K (600 °C), which was applied to the low temperature thermocouple in DHTT experiments.

### 2. Structure analysis

The structure of quenched fluorine-free mold fluxes was examined using Raman spectroscopy (Renishaw inVia Raman Microscope, UK). The amorphous powders used for structure analysis were also prepared by quenching the molten mold fluxes on a copper plate as described in Section II–A. The measurement was conducted at room temperature and the Raman shift ranged from 200 to 1800 cm<sup>-1</sup>. The excitation wavelength of Ar-ion laser was 514 nm with a beam spot size of 1.5 μm. After measurements, the normalized Raman spectra were deconvoluted based on Gaussian distribution using WiRE 3.4 software. The molar fractions of  $Q^n$  species,  $X_n$  [ $n$  (the number of bridging oxygens) = 0, 1, 2, 3, and 4], were calculated by the following equation:

$$X_n = (A_n/S_n) / \left( \sum_{n=0}^4 (A_n/S_n) \right), \quad [3]$$

where  $A_n$  denotes the area of the assigned  $Q^n$  peaks, and  $S_n$  represents the Raman scattering coefficients which equal to 1, 0.514, 0.242, 0.09, and 0.015 when  $n = 0, 1, 2, 3,$  and  $4,$  respectively.<sup>[40–42]</sup>

### 3. Heat transfer tests

Heat flux across the mold flux disk was measured using IET. Mold fluxes were melted in a furnace at 1673 K (1400 °C) for homogenization and then quenched into a cylindrical copper mold with an inner diameter of 40 mm. The flux disk was removed from the mold after solidification and uploaded to another furnace in which the temperature gradually cooled down from 873 K to 573 K (600 °C to 300 °C) to

minimize the stress. Then it was ground and polished to a thickness of 4 mm. The fabricated mold flux disk was placed on top of the copper base, exposed to the infrared radiation. The stepwise power profile of IET tests is presented in Figure 3(d). The system emitted an increasing incident thermal radiation up to 1.6 MW/m<sup>2</sup>, which is close to the radiation released from the steel strand in continuous casting.

## III. RESULTS

### A. Continuous Cooling Experiments

Figures 4(a) to (d) show the CCT diagrams of Samples 1 to 4 with B<sub>2</sub>O<sub>3</sub> content varying from 4.7 to 10.4 mass pct. For given mold fluxes, the crystallization temperature of mold fluxes decreased with increasing cooling rate. For example, the crystallization temperature of Sample 2 (6.8 mass pct B<sub>2</sub>O<sub>3</sub>) declined from 1450 K to 1273 K (1177 °C to 1000 °C) when the cooling rate increased from 1 to 20 K/s. The critical cooling rate, above which crystallization would not take place during continuous cooling process, decreased from 30 to 20, 5, and 1.5 K/s with the increase of B<sub>2</sub>O<sub>3</sub> content from 4.7 to 6.8, 8.6, and 10.4 mass pct, correspondingly. The crystallization temperature of mold fluxes at a given cooling rate also declined with the increasing B<sub>2</sub>O<sub>3</sub> addition as listed in Table II. For the continuous cooling process with a given cooling rate of 1 K/s, the crystallization temperature of mold fluxes decreased from 1497 K to 1312 K (1224 °C to 1039 °C) when B<sub>2</sub>O<sub>3</sub> content increased from 4.7 to 10.4 mass pct as compared in Figure 4(e).

### B. Isothermal Experiments

The TTT diagrams of Samples 1 to 4 with B<sub>2</sub>O<sub>3</sub> content ranging from 4.7 to 10.4 mass pct are presented in Figures 5(a) to (d). The shortest incubation time of mold fluxes increased from nearly 0 second to 1, 17.3, and 79.6 seconds when B<sub>2</sub>O<sub>3</sub> concentration increased from 4.7 to 6.8, 8.6, and 10.4 mass pct; while the highest crystallization temperature of mold fluxes decreased from 1548 K to 1423 K (1275 °C to 1150 °C), 1398 K, and 1323 K (1125 °C and 1050 °C) with the increasing B<sub>2</sub>O<sub>3</sub> concentration from 4.7 to 6.8, 8.6, and 10.4 mass pct, correspondingly, as compared in Figure 5(e). It is noteworthy that crystallization of Sample 1 (B<sub>2</sub>O<sub>3</sub> = 4.7 mass pct) started before the system reached isothermal stage when the target temperature was set below 1398 K (1125 °C) since the cooling process gradually slowed down from 220 to 0 K/s when the real-time temperature was approaching the target temperature.

The XRD patterns of mold fluxes treated at 1173 K and 1273 K (900 °C and 1000 °C) are shown in Figure 6. The dominant phase of mold fluxes with 4.8 mass pct B<sub>2</sub>O<sub>3</sub> (Sample 1) was Ca<sub>2</sub>MgSi<sub>2</sub>O<sub>7</sub> at 1173 K (900 °C) (Figure 6(a)); it changed to CaSiO<sub>3</sub> with the increase of B<sub>2</sub>O<sub>3</sub> concentration. The precipitation of Ca<sub>11</sub>Si<sub>4</sub>B<sub>2</sub>O<sub>22</sub>, a major phase in Sample 1 (4.7 mass pct



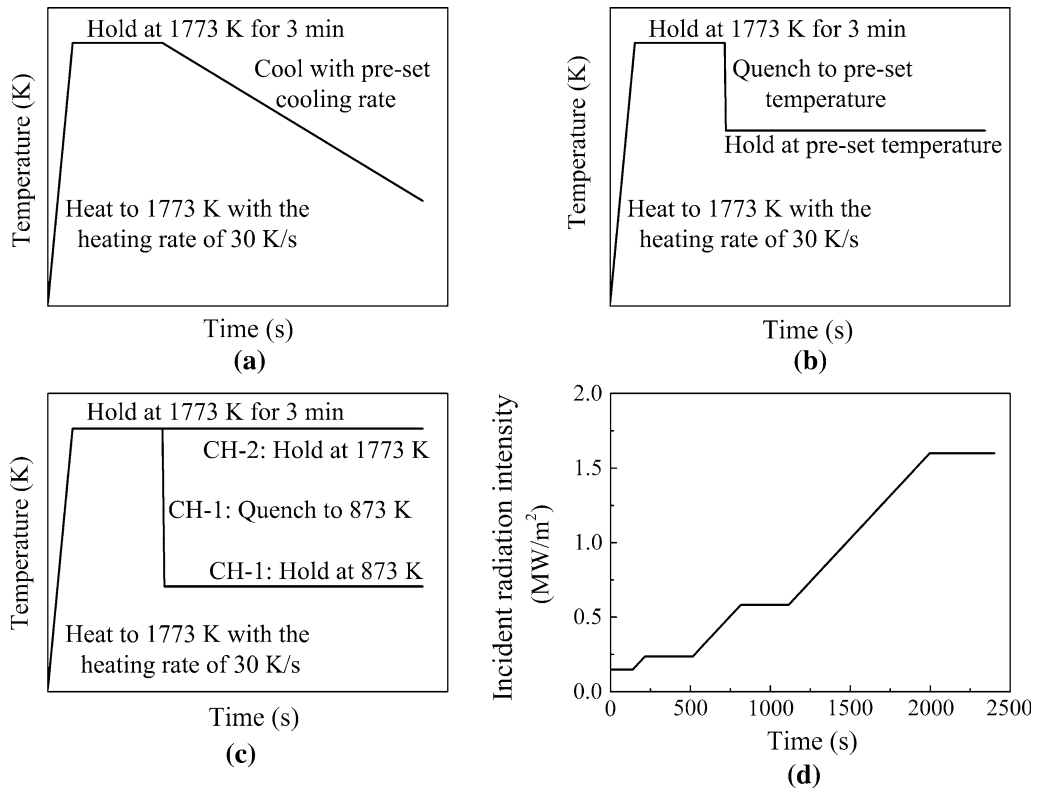


Fig. 3—Schematic temperature profiles in (a) continuous cooling experiments, (b) isothermal experiments, (c) DHTT experiments, and (d) power profile in IET tests.

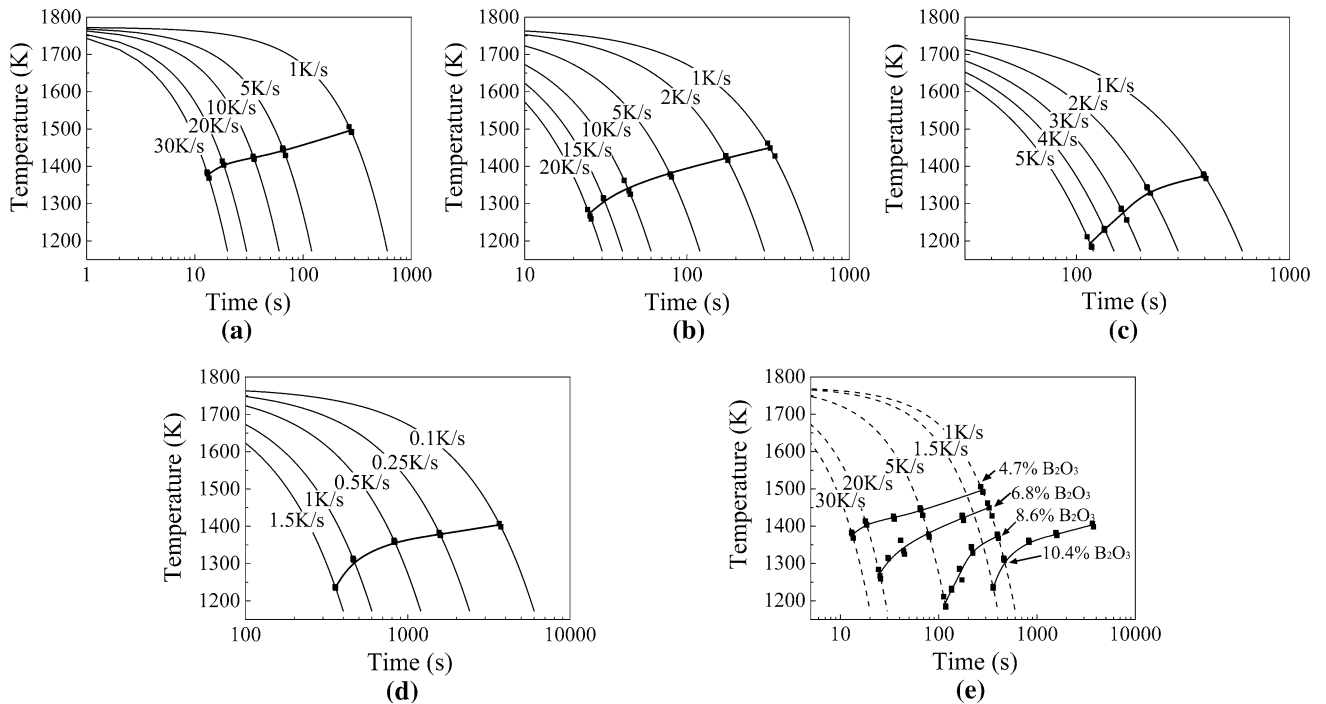


Fig. 4—CCT diagrams of mold fluxes: (a) Sample 1:  $B_2O_3 = 4.7$  mass pct, (b) Sample 2:  $B_2O_3 = 6.8$  mass pct, (c) Sample 3:  $B_2O_3 = 8.6$  mass pct, (d) Sample 4:  $B_2O_3 = 10.4$  mass pct, and (e) comparison of CCT diagrams of Sample 1 to Sample 4.

$B_2O_3$ ), also gradually diminished as  $B_2O_3$  content increased from 4.7 to 10.4 mass pct. Some minor phases were also observed in XRD analysis, such as

$Ca_2Si_3Na_2O_9$  and  $CaTiO_3$ . The precipitated phases of mold fluxes changed in a similar manner at 1273 K (1000 °C) (Figure 6(b)).  $CaSiO_3$  was the major phase in

**Table II. Average Crystallization Temperatures [K (°C)] of Mold Fluxes in Continuous Cooling Experiments**

Cooling Rate [K (°C)/s]	Sample			
	1 (4.7 Pct B <sub>2</sub> O <sub>3</sub> )	2 (6.8 Pct B <sub>2</sub> O <sub>3</sub> )	3 (8.6 Pct B <sub>2</sub> O <sub>3</sub> )	4 (10.4 Pct B <sub>2</sub> O <sub>3</sub> )
0.1				1404 (1131)
0.25				1378 (1105)
0.5				1360 (1087)
1	1497 (1224)	1450 (1177)	1374 (1101)	1312 (1039)
1.5				1236 (963)
2		1423 (1150)	1339 (1066)	
3			1275 (1002)	
4			1231 (958)	
5	1441 (1168)	1383 (1110)	1193 (920)	
10	1423 (1150)	1343 (1070)		
15		1308 (1035)		
20	1407 (1134)	1273 (1000)		
30	1377 (1104)			

all the samples. The precipitation of Ca<sub>11</sub>Si<sub>4</sub>B<sub>2</sub>O<sub>22</sub> and Ca<sub>2</sub>MgSi<sub>2</sub>O<sub>7</sub> decreased with the increase of B<sub>2</sub>O<sub>3</sub> content; while an increasing amount of CaSiO<sub>3</sub> was observed when B<sub>2</sub>O<sub>3</sub> content increased from 4.7 to 10.4 mass pct. The amount of Ca<sub>11</sub>Si<sub>4</sub>B<sub>2</sub>O<sub>22</sub> was also very significant when B<sub>2</sub>O<sub>3</sub> content was low but it decreased gradually with the increase of B<sub>2</sub>O<sub>3</sub> content. Ca<sub>2</sub>MgSi<sub>2</sub>O<sub>7</sub> was only observed in Sample 1 (4.7 mass pct B<sub>2</sub>O<sub>3</sub>) at 1273 K (1000 °C). Minor precipitates, Ca<sub>2</sub>Si<sub>3</sub>Na<sub>2</sub>O<sub>9</sub> and CaTiO<sub>3</sub>, were also found at 1273 K (1000 °C).

### C. Double Hot Thermocouple Technique Experiments

Figure 7 shows the crystallization behavior of mold fluxes with different B<sub>2</sub>O<sub>3</sub> content in a thermal field simulating the temperature gradient between steel strand and copper mold near meniscus zone. Crystallization of Sample 1 (B<sub>2</sub>O<sub>3</sub> = 4.7 mass pct) started in the center of flux film where the cooling condition was relatively mild during cooling stage. Some crystals formed in the relatively lower temperature zone were immediately frozen; while the other nuclei propagated to form a thin crystalline layer with a crystallinity of 28.9 pct within only 10 seconds under the temperature gradient (Figure 7(a1)). Then the crystalline layer promptly stretched to both high and low temperature zones with a high crystallization rate; the crystallinity of Sample 1 reached 54.4 pct in 60 seconds (Figure 7(a2)). It is noteworthy that a large number of equiaxed crystals formed at liquid/crystalline interface were drifted by Marangoni flow and finally melted at the high temperature zone which made the propagation of crystalline layer unstable in this temperature region. Then the crystallization process reached a relatively stable stage with a low crystalline growth rate. The crystallinity of the flux film gradually increased to 61.2 pct at 300 seconds (Figure 7(a3)) and 73.3 pct at 600 seconds (Figure 7(a4)).

Figures 7(b1) to 7(b4) show the crystallization behavior of Sample 2 (B<sub>2</sub>O<sub>3</sub> = 6.8 mass pct) in the same thermal condition. Several crystals precipitated in the middle of flux film at 10 seconds after the cold side

entered the isothermal stage (Figure 7(b1)). But unlike Sample 1, a distinct crystalline layer was not observed in Sample 2 at this time. A solid crystalline layer was observed with a crystallinity of 46.2 pct at 60 seconds (Figure 7(b2)). Likewise, the crystallization process slowed down after 300 seconds (Figures 7(b3) and (b4)).

Sample 3 (B<sub>2</sub>O<sub>3</sub> = 8.6 mass pct) exhibited a weaker crystallization tendency as shown in Figures 7(c1) to 7(c4). Few nuclei could be traced for the time of 60 seconds. A thin crystalline layer was gradually formed before 300 seconds and steadily developed into a thick crystalline layer with the crystallinity of 63.6 pct at 900 seconds. Figures 7(d1) to 7(d4) show the crystallinity evolution of Sample 4 (B<sub>2</sub>O<sub>3</sub> = 10.4 mass pct) in the DHTT experiments. Crystallization took place at around 600 seconds, the longest incubation time of all the samples. The crystalline layer gradually formed after 900 seconds and established a distinct liquid/crystalline/glass structure. It is noted that the position of crystalline/liquid interface moved to the lower temperature side with the increase of B<sub>2</sub>O<sub>3</sub> content at given reaction time, *e.g.*, 600 seconds, as the melting temperature decreased with increasing B<sub>2</sub>O<sub>3</sub> content.

### D. Raman Spectroscopy

Raman spectra of Samples 1 to 4 in a truncated frequency range of 600 to 1550 cm<sup>-1</sup> are displayed in Figure 8. The Raman envelope was further deconvoluted as indicated in Figure 9. The recommended assignments of Raman peaks are summarized in Table III with relevant references.<sup>[40,43–54]</sup> Two peaks around 705 and 810 cm<sup>-1</sup> were assigned to the deformation of O-Ti-O or O-(Si, Ti)-O in chain or sheet units or both,<sup>[47–50]</sup> and the stretching vibration of Ti-O in TiO<sub>4</sub><sup>4-</sup> monomers,<sup>[47–49]</sup> respectively, due to the strong influence of TiO<sub>2</sub>. The areas of Ti-related peaks were not significantly changed with the addition of B<sub>2</sub>O<sub>3</sub> although the peak at 803 cm<sup>-1</sup> was somehow slightly smaller than the counterparts in other samples. The peak located around 660 cm<sup>-1</sup> was assigned to B-O-B stretching in ring/chain-type metaborate units.<sup>[43–46]</sup> Another borate-related peak was centered near 1185 cm<sup>-1</sup> indicating the B-O stretching in

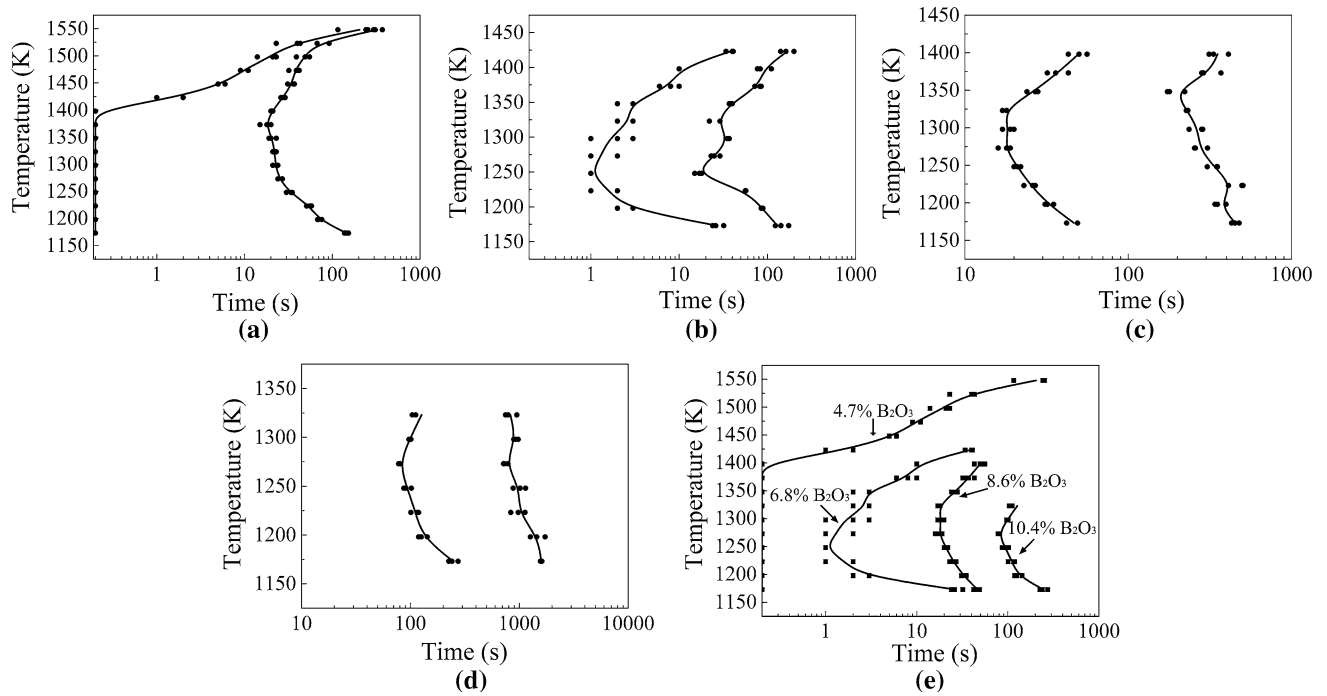


Fig. 5—TTT diagrams of mold fluxes: (a) Sample 1:  $B_2O_3 = 4.7$  mass pct, (b) Sample 2:  $B_2O_3 = 6.8$  mass pct, (c) Sample 3:  $B_2O_3 = 8.6$  mass pct, (d) Sample 4:  $B_2O_3 = 10.4$  mass pct, and (e) comparison of TTT diagrams (onset of crystallization) of Sample 1 to Sample 4.

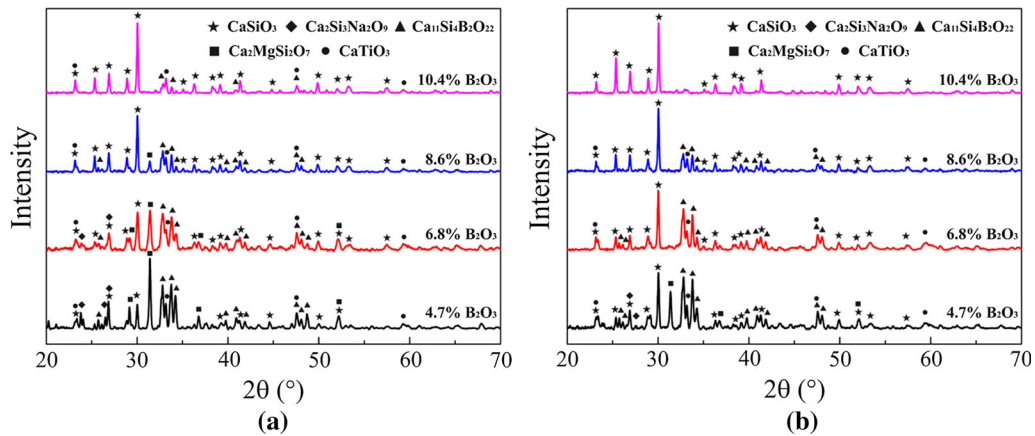


Fig. 6—XRD patterns of mold fluxes with different  $B_2O_3$  content treated at (a) 1173 K (900 °C) and (b) 1273 K (1000 °C).

$BO_4$  tetrahedral units; while the two bands located around  $1360$  and  $1450\text{ cm}^{-1}$  were assigned to B-O stretching vibration in  $BO_3$  trigonal units connected to  $BO_4$  tetrahedral units or other large borate groups in a high frequency region.<sup>[40,44,45,50,52–54]</sup> The amount of borate structure all increased with the addition of  $B_2O_3$  with respect to their peak areas. The percentage of  $BO_4$  tetrahedral units was higher than that of  $BO_3$  trigonal-related units which was even absent in Sample 1 ( $B_2O_3 = 4.7$  mass pct). The Raman envelope between  $800$  and  $1100\text{ cm}^{-1}$  was assigned to silicate groups. It was deconvoluted into  $Q^0$ ,  $Q^1$ ,  $Q^2$ , and  $Q^3$ .<sup>[40,47,50,51]</sup>  $Q^4$  ( $SiO_2$  net) was not distinguishable in the Raman Spectra (*ca.*  $1100$  to  $1150\text{ cm}^{-1}$ <sup>[22]</sup>) due to its low intensity. The molar fractions of silicate units are shown in Figure 10.

The major unit in the silicate structure was  $Q^2$  ( $SiO_3^{2-}$ ); its molar fraction was 71 pct in the fluxes with 4.8 mass pct  $B_2O_3$ ; it decreased to 61 pct with increasing  $B_2O_3$  concentration to 8.6 mass pct, and did not change with the further increase of  $B_2O_3$  concentration to 10.4 mass pct. The molar fractions of  $Q^0$  ( $SiO_4^{4-}$ ) decreased, but  $Q^3$  ( $Si_2O_5^{2-}$ ) increased with the increase of  $B_2O_3$  concentration until 8.6 mass pct; while the variation of  $Q^1$  ( $Si_2O_7^{6-}$ ) as a function of  $B_2O_3$  concentration was not distinct. The molar fraction change of silicate units became insignificant when  $B_2O_3$  content increased from 8.6 to 10.4 mass pct. It is assumed that the incorporation of  $B_2O_3$  into the silicate structure reached saturation due to the limited space around the complicated silicate network.

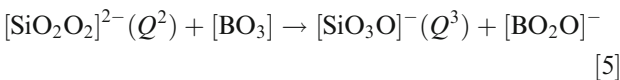
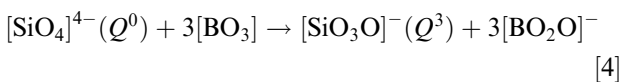
### E. Heat Transfer Tests

The responding heat flux across the disks of mold fluxes with different B<sub>2</sub>O<sub>3</sub> content in the IET experiments is shown in Figure 11(a). The upper part of the flux disk upon heating by the infrared radiation started to melt and then formed a dome at high temperatures; while the lower part of the flux disk got crystallized and became opaque as the experiment proceeded. Since the thermocouples embedded in copper base are insensitive to the temperature change at low temperatures, the recorded responding temperatures in the first 600 seconds were not reliable for the calculation of heat flux. The responding heat flux increased with the increasing infrared radiation intensity. Heat transfer properties of different samples were compared when the incident radiation intensity reached 1.6 MW/m<sup>2</sup>. At this stage, the heat flux decreased from 659 to 595 kW/m<sup>2</sup> when B<sub>2</sub>O<sub>3</sub> content increased from 4.7 to 6.8 mass pct; while a further increase of B<sub>2</sub>O<sub>3</sub> concentration from 6.8 to 8.6 and 10.4 mass pct raised the heat flux from 595 to 712 and 736 kW/m<sup>2</sup>, respectively. Heat flux of fluorine-free mold fluxes is compared with that of industrial fluorine-containing mold fluxes under the same incident radiation of 1.6 MW/m<sup>2</sup><sup>[17]</sup> in Figure 11(b). A responding heat flux for Sample 2 (B<sub>2</sub>O<sub>3</sub> = 6.8 mass pct) was closest to the heat flux of fluorine-containing fluxes.

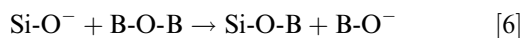
## IV. DISCUSSION

### A. Effect of B<sub>2</sub>O<sub>3</sub> on the Structure of Mold Fluxes

The addition of B<sub>2</sub>O<sub>3</sub> influences the melt structure mainly in two ways: (1) changing silicate structure by reacting with non-bridging oxygen (NBO),<sup>[22,40,43,50,52,55]</sup> and (2) increasing the degree of polymerization by forming 3D borate structural groups.<sup>[22,43,50]</sup> As indicated in Figures 9 and 10, the addition of B<sub>2</sub>O<sub>3</sub> facilitated the formation of Q<sup>3</sup> units at the cost of the reduction of Q<sup>0</sup> and Q<sup>2</sup> units. Similar observation was also reported in works.<sup>[40,55]</sup> The formation of Q<sup>3</sup> units with an increasing amount of bridging oxygen may occur according to the following reactions<sup>[40]</sup>:



Likewise, Si-O-B bonding was also formed<sup>[40]</sup>:



Moreover, B<sub>2</sub>O<sub>3</sub> reacts with network-modifying oxides to retain more bridging oxygen in the silicate structure.<sup>[50]</sup> B<sub>2</sub>O<sub>3</sub> also brought in both BO<sub>4</sub> tetrahedral and BO<sub>3</sub> trigonal units as indicated in high frequency region of Raman envelopes (Figure 9; Table III). BO<sub>3</sub> trigonal units may form 2D groups such as boroxol

rings but BO<sub>4</sub> units are most likely to interconnect BO<sub>3</sub> trigonal units forming a complex 3D structure.<sup>[22,52]</sup> Without the involvement of BO<sub>3</sub> trigonal units, the individual existence of BO<sub>4</sub> tetrahedral units normally does not facilitate the formation of 3D structure due to the avoidance effect of BO<sub>4</sub> groups.<sup>[56,57]</sup> It means that BO<sub>4</sub> tetrahedra were not preferred to interconnect each other but be isolated by BO<sub>3</sub> trigonal units in 3D borate structure. As a result, the degree of polymerization increased with the addition of B<sub>2</sub>O<sub>3</sub>, which is consistent with the acidic nature of B<sub>2</sub>O<sub>3</sub> acting as a network former in flux melts.<sup>[1]</sup>

### B. Effect of B<sub>2</sub>O<sub>3</sub> on the Crystallization Behavior of Mold Fluxes

The addition of B<sub>2</sub>O<sub>3</sub> decreased the critical cooling rate of mold fluxes from 30 to 1.5 K/s in the continuous cooling experiments (Figure 4), and raised the shortest incubation time from nearly 0 to 79.6 seconds in the isothermal experiments (Figure 5). The time that mold flux films require to reach certain crystallinity increased with the increasing B<sub>2</sub>O<sub>3</sub> content (Figure 7). It implies that the addition of B<sub>2</sub>O<sub>3</sub> inhibited crystallization process of mold fluxes in present study. The same effect of B<sub>2</sub>O<sub>3</sub> was reported for the fluoride-containing mold fluxes.<sup>[13,23]</sup> The maximal cooling rate in meniscus region during continuous casting operation was reported to be 20 K/s.<sup>[31,32]</sup> In this way, Samples 1 and 2 (B<sub>2</sub>O<sub>3</sub> = 4.7 and 6.8 mass pct) are expected to crystallize directly from the molten state when they infiltrate into the interface between copper mold and steel strand; while Samples 3 and 4 (B<sub>2</sub>O<sub>3</sub> = 8.6 and 10.4 mass pct) are likely to freeze into vitreous state when they encounter copper mold. Empirically, the mold fluxes with high crystallization tendency (Samples 1 and 2) are suitable for the casting of cracking-sensitive steel that requires mild cooling conditions in meniscus region; those with low crystallization tendency (Samples 3 and 4) can be used for the casting of sticking-sensitive steel that requires adequate lubricity. Figure 12 compares the TTT diagrams of the fluorine-free mold fluxes with the industrial mold fluxes for the casting of low-carbon (LC) steel and medium-carbon (MC) steel.<sup>[38,58]</sup> It clearly shows that the crystallization behavior of Sample 1 is similar to that of the mold fluxes for the medium-carbon steel casting; while the crystallization tendencies of Samples 3 and 4 are close to those for the low-carbon steel casting.

The addition of B<sub>2</sub>O<sub>3</sub> lowers the melting temperature of mold fluxes,  $T_m$ , as indicated by the hemisphere temperature in Table I and data in the references.<sup>[10,25,59]</sup> In the process of crystallization at temperature  $T$ , the undercooling of mold fluxes,  $\Delta T = T_m - T$ , decreases with the increase in B<sub>2</sub>O<sub>3</sub> content. The net change in energy for nucleus of critical size,  $W^*$ , *i.e.*, the thermodynamic barrier to nucleation, is defined by the expression<sup>[60]</sup>:

$$W^* = \frac{16\pi\gamma^3 T_m^2}{3H_f^2} \cdot \frac{1}{(\Delta T)^2}, \quad [7]$$



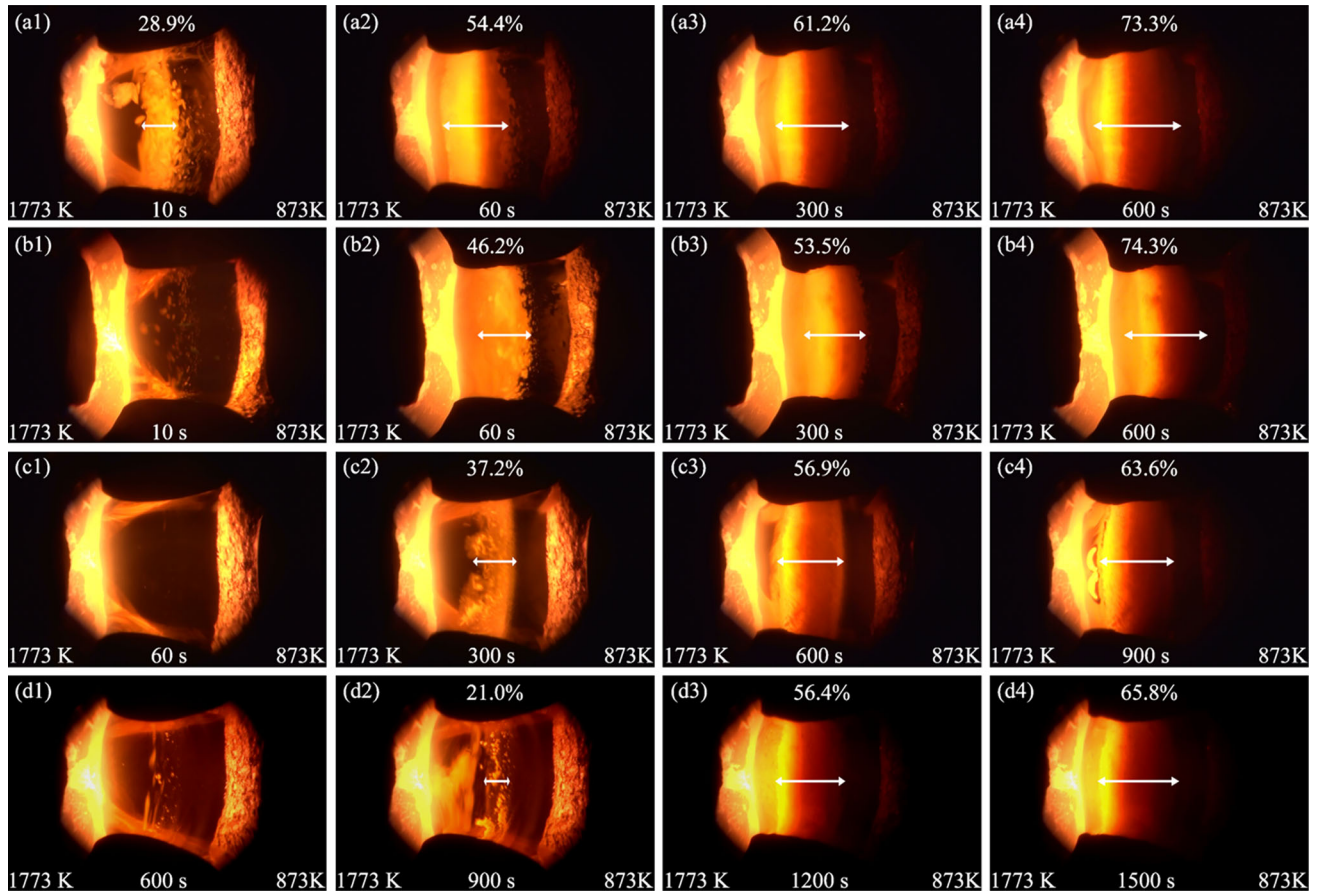


Fig. 7—Crystallization process of mold fluxes in DHTT experiments: (a1) to (a4): Sample 1 ( $B_2O_3 = 4.7$  mass pct) at 10, 60, 300, and 600 s; (b1) to (b4): Sample 2 ( $B_2O_3 = 6.8$  mass pct) at 10, 60, 300, and 600 s; (c1) to (c4): Sample 3 ( $B_2O_3 = 8.6$  mass pct) at 60, 300, 600, and 900 s; (d1) to (d4): Sample 4 ( $B_2O_3 = 10.4$  mass pct) at 600, 900, 1200, and 1500 s. (The fractions of the crystalline layer at given times are given on the top of images).

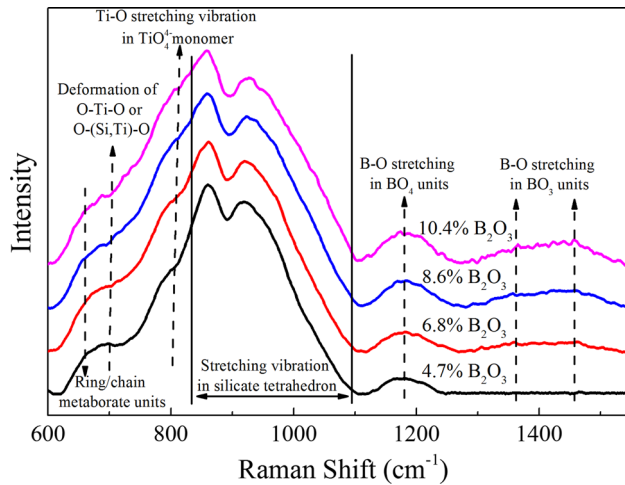


Fig. 8—Raman spectra of mold fluxes with  $B_2O_3$  content varying from 4.7 to 10.4 mass pct.

where  $\gamma$  is the crystal/melt interfacial free energy per unit area, and  $H_f$  is the latent heat of fusion per unit volume. It can be readily transformed to the following equation:

$$W^* = \frac{16\pi\gamma^3}{3H_f^2} \cdot \left(1 + \frac{T}{T_m - T}\right)^2 \quad [8]$$

As the undercooling of mold fluxes became larger at given temperatures due to the decline in the melting temperature with increasing  $B_2O_3$  content from 4.7 to 10.4 mass pct, the thermodynamic barrier of the system to nucleation increased. Therefore, the addition of  $B_2O_3$  made the nucleation process thermodynamically more difficult.

The overall nucleation process is related to not only the energy for the formation of nucleus with critical size,  $W^*$ , but also the activation energy for ionic migration,  $\Delta G_D$ , which can be described by the following equation<sup>[60]</sup>:

$$\Delta G_D = kT \ln \left( \frac{kT\lambda^2}{h \cdot D} \right), \quad [9]$$

where  $D$  denotes effective diffusion coefficient,  $k$  is Boltzmann constant,  $T$  is the absolute temperature,  $h$  is Planck constant, and  $\lambda$  represents the atomic jump distance. It is known that the addition of  $B_2O_3$  to silicate mold fluxes decreases flux viscosity.<sup>[22,24,29,52,61]</sup>

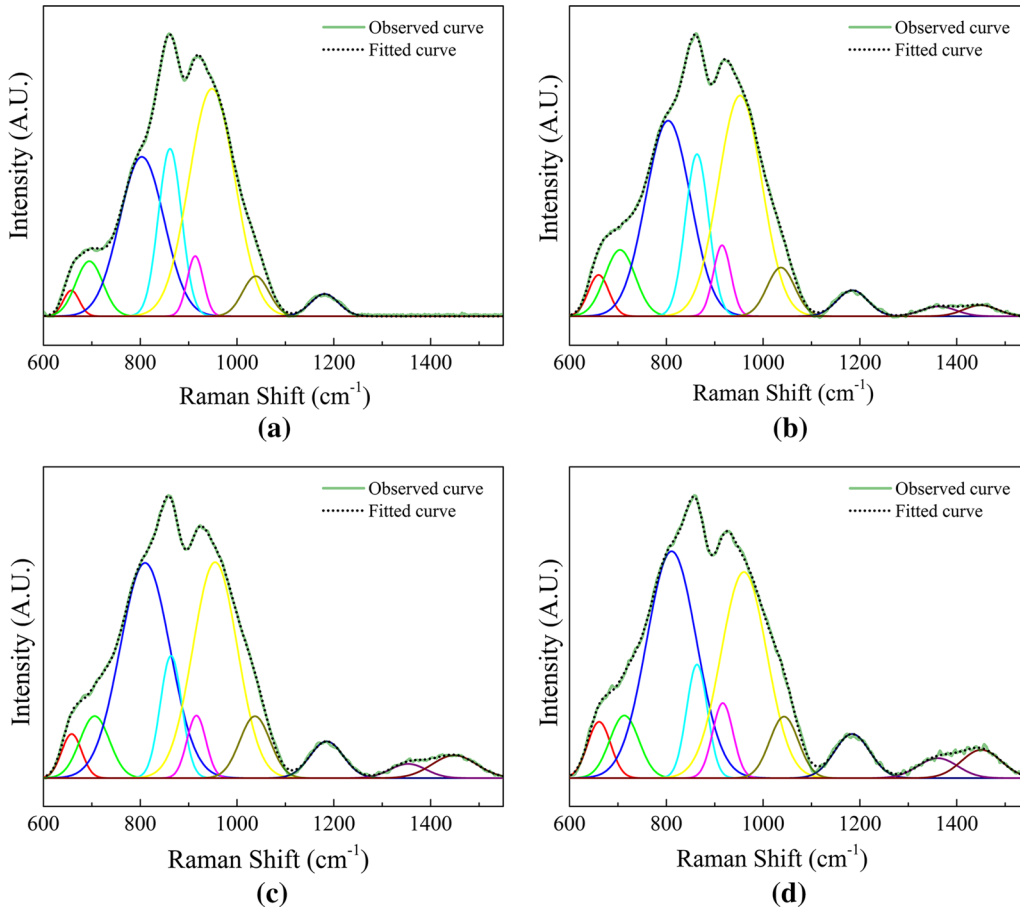


Fig. 9—Deconvoluted Raman spectra of mold fluxes with different  $B_2O_3$  content in a truncated frequency range of 600 to 1550  $cm^{-1}$ : (a) Sample 1 ( $B_2O_3 = 4.7$  mass pct), (b) Sample 2 ( $B_2O_3 = 6.8$  mass pct), (c) Sample 3 ( $B_2O_3 = 8.6$  mass pct), and (d) Sample 4 ( $B_2O_3 = 10.4$  mass pct).

Wang *et al.*<sup>[61]</sup> carried out the measurement of viscosity of a similar flux system, indicating that the viscosity at 1473 K (1200 °C) decreased from 1.369 Pa s to 0.995, 0.907, and 0.766 Pa s with increasing  $B_2O_3$  content from 3 wt pct to 5, 7, and 10 wt pct due to the melting property changes. Ionic diffusion in flux melts is related to viscosity according to Stokes–Einstein equation:

$$D = \frac{kT}{3\pi\lambda\eta} \quad [10]$$

Therefore, it can be expected that the increase of  $B_2O_3$  content from 4.7 to 10.4 mass pct increased the ionic diffusion and decreased  $\Delta G_D$  in studied mold flux. Some works<sup>[13,23,62,63]</sup> claim that the flux polymerization induced by  $B_2O_3$  could decrease the ionic diffusion in melts and increase  $\Delta G_D$ . The degree of polymerization indeed increased with increasing amount of  $B_2O_3$  as shown by Raman analysis. However, if we assume that the flux polymerization caused the retardation of ionic diffusion, then the flux viscosity should increase with increasing amount of  $B_2O_3$ , which is apparently contrary to the experimental fact that the viscosity decreases with the addition of  $B_2O_3$ . Therefore, it can be concluded that it is the melting property change rather than the structural complexity that plays a predominant role

in governing the ionic diffusion, which leads to the decrease of  $\Delta G_D$ .

The overall nucleation rate,  $I$ , is defined by the expression<sup>[60]</sup>:

$$I = A \exp \frac{-(W^* + \Delta G_D)}{kT}, \quad [11]$$

where  $A$  is a pre-exponential constant. As discussed above, the addition of  $B_2O_3$  leads to an increase in  $W^*$  but a decrease in  $\Delta G_D$ . The observed reducing crystallization tendency with increasing  $B_2O_3$  content indicates a decrease in the nucleation rate,  $I$ . It means that the retardation effect caused by the increasing thermodynamic barrier,  $W^*$ , dominates over the decreasing kinetic barrier,  $\Delta G_D$ . Therefore, a synergic effect led to the decrease of nucleation rate of mold fluxes when  $B_2O_3$  content increased. Likewise, the crystal growth rate,  $U$ , is described by<sup>[60]</sup>:

$$U = B \exp \frac{-\Delta E}{kT} \left( 1 - \exp \frac{\Delta G}{kT} \right), \quad [12]$$

where  $B$  is a pre-exponential constant related to the interatomic separation distance and the vibrational frequency,  $\Delta E$  is the kinetic barrier to crystal growth, and  $\Delta G$  is the thermodynamic barrier to crystal growth. The changes of  $\Delta E$  and  $\Delta G$  as a function of

B<sub>2</sub>O<sub>3</sub> follow the similar way as to  $\Delta G_D$  and  $W^*$  in the description of the nucleation rate. Therefore, the effect of B<sub>2</sub>O<sub>3</sub> on crystal growth resembles that on nucleation. The addition of B<sub>2</sub>O<sub>3</sub> retarded the crystallization process of the studied mold fluxes.

### C. Precipitates Formed in the Crystallization Process

Figure 6 shows that the major precipitates of mold fluxes at 1173 K and 1273 K (900 °C and 1000 °C) included CaSiO<sub>3</sub>, Ca<sub>2</sub>MgSi<sub>2</sub>O<sub>7</sub>, and Ca<sub>11</sub>Si<sub>4</sub>B<sub>2</sub>O<sub>22</sub>. Minor precipitates, such as Ca<sub>2</sub>Si<sub>3</sub>Na<sub>2</sub>O<sub>9</sub> and CaTiO<sub>3</sub>, were also found in the XRD analysis. As shown in Figure 6, the increase of B<sub>2</sub>O<sub>3</sub> content suppressed the formation of Ca<sub>11</sub>Si<sub>4</sub>B<sub>2</sub>O<sub>22</sub> and promoted the precipitation of CaSiO<sub>3</sub>. Since 1 mole Ca<sub>11</sub>Si<sub>4</sub>B<sub>2</sub>O<sub>22</sub> (925.6 g) only comprises approximately 7.5 mass pct B<sub>2</sub>O<sub>3</sub> (69.6 g), the concentration of B<sub>2</sub>O<sub>3</sub> may not be a decisive factor in the formation of Ca<sub>11</sub>Si<sub>4</sub>B<sub>2</sub>O<sub>22</sub>. The increase of B<sub>2</sub>O<sub>3</sub> content made the formation of Ca<sub>11</sub>Si<sub>4</sub>B<sub>2</sub>O<sub>22</sub> thermodynamically difficult which will be addressed

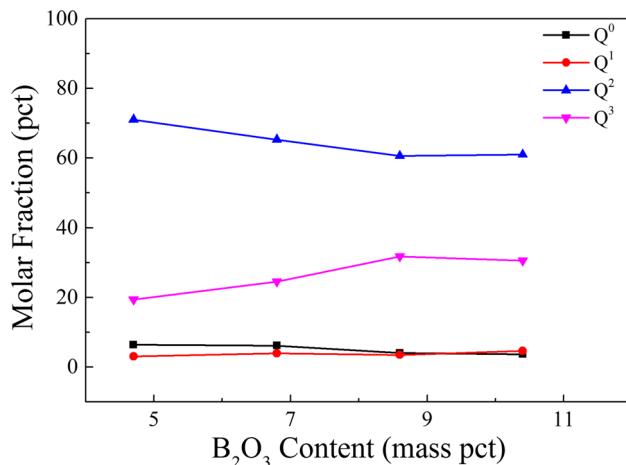


Fig. 10—Molar fraction of  $Q^n$  ( $n = 0, 1, 2,$  and  $3$ ) units in fluxes with varied B<sub>2</sub>O<sub>3</sub> contents.

below. The precipitation of Ca<sub>11</sub>Si<sub>4</sub>B<sub>2</sub>O<sub>22</sub> was observed in the mold fluxes with low B<sub>2</sub>O<sub>3</sub> content especially at a higher temperature that facilitated the crystallization process of mold fluxes.<sup>[13,15,17]</sup> Figure 6 also indicates that Ca<sub>2</sub>MgSi<sub>2</sub>O<sub>7</sub> was sensitive to the annealing temperature; it was a major phase at 1173 K (900 °C) when B<sub>2</sub>O<sub>3</sub> content was lower than 6.8 mass pct; while no trace of Ca<sub>2</sub>MgSi<sub>2</sub>O<sub>7</sub> was found at 1273 K (1000 °C) except Sample 1 (B<sub>2</sub>O<sub>3</sub> = 4.7 mass pct).

The equilibrium phases of mold fluxes were determined by the thermodynamic calculation using FactSage 7.0. Figure 13 shows the predicted phase fractions from 1073 K to 1573 K (800 °C to 1300 °C). Li<sub>2</sub>O was not considered in the calculation since its database is not applicable in the current FactSage package. The predicted phases included CaSiO<sub>3</sub>, Ca<sub>11</sub>Si<sub>4</sub>B<sub>2</sub>O<sub>22</sub>, Ca<sub>2</sub>MgSi<sub>2</sub>O<sub>7</sub>, Ca<sub>2</sub>Si<sub>3</sub>Na<sub>2</sub>O<sub>9</sub>, and CaTiO<sub>3</sub>, which are consistent with the XRD analysis. The percentage of CaSiO<sub>3</sub> (wollastonite) is expected to rise with the increasing concentration of B<sub>2</sub>O<sub>3</sub>; while the concentrations of Ca<sub>11</sub>Si<sub>4</sub>B<sub>2</sub>O<sub>22</sub> and Ca<sub>2</sub>MgSi<sub>2</sub>O<sub>7</sub> (akermanite) are predicted to drop with the increasing concentration of B<sub>2</sub>O<sub>3</sub>. Neither Ca<sub>11</sub>Si<sub>4</sub>B<sub>2</sub>O<sub>22</sub> nor Ca<sub>2</sub>MgSi<sub>2</sub>O<sub>7</sub> is present in the thermodynamic model of Sample 4 (B<sub>2</sub>O<sub>3</sub> = 10.4 mass pct). The percentage of CaTiO<sub>3</sub> slightly declines with the addition of B<sub>2</sub>O<sub>3</sub>. These predictions correctly reflect the variation trends in the XRD patterns as shown in Figure 6. Moreover, the crystalline evolution also indicates that the increase of B<sub>2</sub>O<sub>3</sub> restrained the crystallization fraction at given temperatures, implying a decreasing crystallization tendency. It confirms that the addition of B<sub>2</sub>O<sub>3</sub> thermodynamically inhibited the crystallization process of mold fluxes. But Ca<sub>2</sub>Si<sub>3</sub>Na<sub>2</sub>O<sub>9</sub> (combeite) was a minor precipitate in the XRD analysis and it even did not exist in the mold fluxes with high concentration of B<sub>2</sub>O<sub>3</sub>. It is different from the thermodynamic prediction in which Ca<sub>2</sub>Si<sub>3</sub>Na<sub>2</sub>O<sub>9</sub> is the major phase in all the samples. It is noteworthy that Ca<sub>2</sub>MgSi<sub>2</sub>O<sub>7</sub> is converted to Ca<sub>3</sub>MgSi<sub>2</sub>O<sub>8</sub> (merwinite) at high temperatures in equilibrium state but Ca<sub>3</sub>MgSi<sub>2</sub>O<sub>8</sub> might be unstable in the heat treatment so it could not be reflected in the

Table III. Recommended Assignments of the Peaks in Raman Spectroscopy

	B <sub>2</sub> O <sub>3</sub> Mass Pct				Assignment	Reference
	4.7	6.8	8.6	10.4		
Raman Shifts	657.6	660.2	658.4	661.2	ring/chain-type metaborate units	43–46
Center (cm <sup>-1</sup> )	694.9	704.4	705.9	713.3	deformation of O-Ti-O or O-(Si, Ti)-O in chain or sheet units or both	47–50
	803.4	803.9	809.9	811.0	stretching vibration of Ti-O in TiO <sub>4</sub> <sup>4-</sup> monomers	47–49
	861.6	863.4	863.7	863.4	stretching vibration of silicate tetrahedron without bridging oxygen (Q <sup>0</sup> )	40,47,51
	913.7	915.2	916.1	916.7	stretching vibration of silicate tetrahedron with 1 bridging oxygen (Q <sup>1</sup> )	40,47,51
	948.3	952.6	954.80	960.4	stretching vibration of silicate tetrahedron with 2 bridging oxygen (Q <sup>2</sup> )	40,47,50,51
	1038.8	1036.7	1037.1	1043.2	stretching vibration silicate tetrahedron with 3 bridging oxygen (Q <sup>3</sup> )	40,47,50,51
	1180.9	1184.4	1185.1	1183.9	B-O stretching in BO <sub>4</sub> units	40,44
	—	1362.8	1353.4	1360.9	B-O stretching in BO <sub>3</sub> groups attached to large borate groups	40,45,50,52–54
	—	1449.3	1449.0	1450.9		

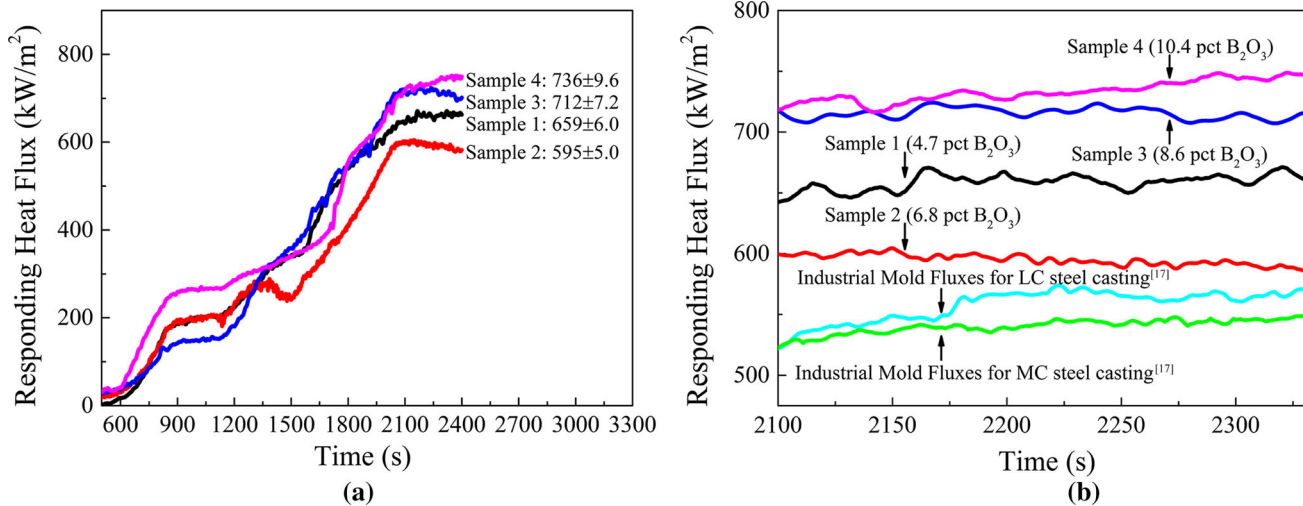


Fig. 11—(a) Heat flux of mold fluxes with different  $B_2O_3$  content, (b) Comparison of heat flux of fluorine-free mold fluxes and industrial mold fluxes under an incident radiation of  $1.6 \text{ MW/m}^2$ .

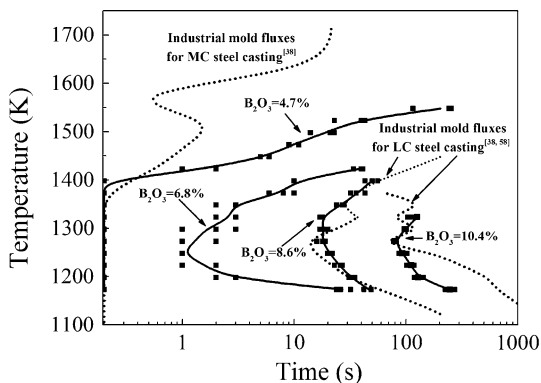


Fig. 12—Comparison of TTT diagrams of fluorine-free mold fluxes and industrial mold fluxes (dotted curves).

XRD patterns. Magnesium and calcium borates, *e.g.*,  $Mg_3B_2O_6$ ,  $Mg_2B_2O_5$ ,  $Ca_3B_2O_6$ , and  $Ca_2B_2O_5$ , which are predicted to precipitate in the low temperature range in small amounts, were not observed in XRD analysis due to low intensity. The thermodynamic analysis presents the equilibrium phases on the basis of the Gibbs free energy calculations; while the crystallization of mold fluxes in experiments occurred under non-equilibrium conditions. The chemistry change in the liquid caused by segregation and the availability of nucleation sites would affect the solidification behavior of the melts to some extent. Therefore, the precipitated phases might differ from those expected in the phase diagram.<sup>[6]</sup> Nevertheless, thermodynamic analysis provides useful references in the flux design and the interpretation of experimental results.

#### D. Relationship between Heat Transfer and Crystallization Behavior of Mold Fluxes

Heat transfer is closely related to the crystallization of mold fluxes. Generally, the increase of crystallization tendency reduces heat flux because of the scattering

effect of grain boundaries and the high thermal resistances of the air gaps caused by surface roughness and cracks. Since  $B_2O_3$  generally inhibits crystallization process, it is reported to promote the radiative heat transfer of mold fluxes.<sup>[23,62]</sup> As discussed above, the crystallization tendency decreased with the increasing amount of  $B_2O_3$  from 4.7 to 10.4 mass pct. In this way, heat flux is expected to increase all the way with the increasing concentration of  $B_2O_3$ . The results of heat flux measurements using IET (Figure 11) demonstrate that the heat flux across the flux disk increased with increasing  $B_2O_3$  content from 6.8 to 10.4 mass pct; however, it decreased when  $B_2O_3$  content increased from 4.7 to 6.8 mass pct. The unexpected drop of heat flux can be attributed to the crystal morphology in the crystalline layer.

Samples 1 and 2 could start crystallization directly from liquid state with a relatively high rate. The increase of  $B_2O_3$  from 4.7 to 6.8 mass pct did not make a significant difference in crystallization as compared with other samples in continuous cooling and isothermal experiments. Figure 14 compares the crystallinity evolution of Samples 1 to 4 in DHTT experiments. Samples 1 and 2 had similar crystallinity which is much higher than Samples 3 and 4. Therefore, the effect of crystallinity on heat transfer was expected to become less important when comparing Samples 1 and 2.

Figure 15 shows the microstructures of liquid/crystalline interface of the flux film in DHTT experiments. A considerable portion of equiaxed crystals formed in Sample 1 ( $B_2O_3 = 4.7$  mass pct) at the liquid/crystalline interface (Figure 15(a)). They were highly dispersive and could be driven easily by Marangoni flow due to the weak connection to the solid crystalline layer. In contrast, dendritic crystals with stronger bonding force with solid crystalline layer were observed at the liquid/crystalline interface of Sample 2 ( $B_2O_3 = 6.8$  mass pct) although some equiaxed crystals also co-existed with dendrites (Figure 15(b)). The equiaxed crystals with high mobility are strongly prone to Marangoni



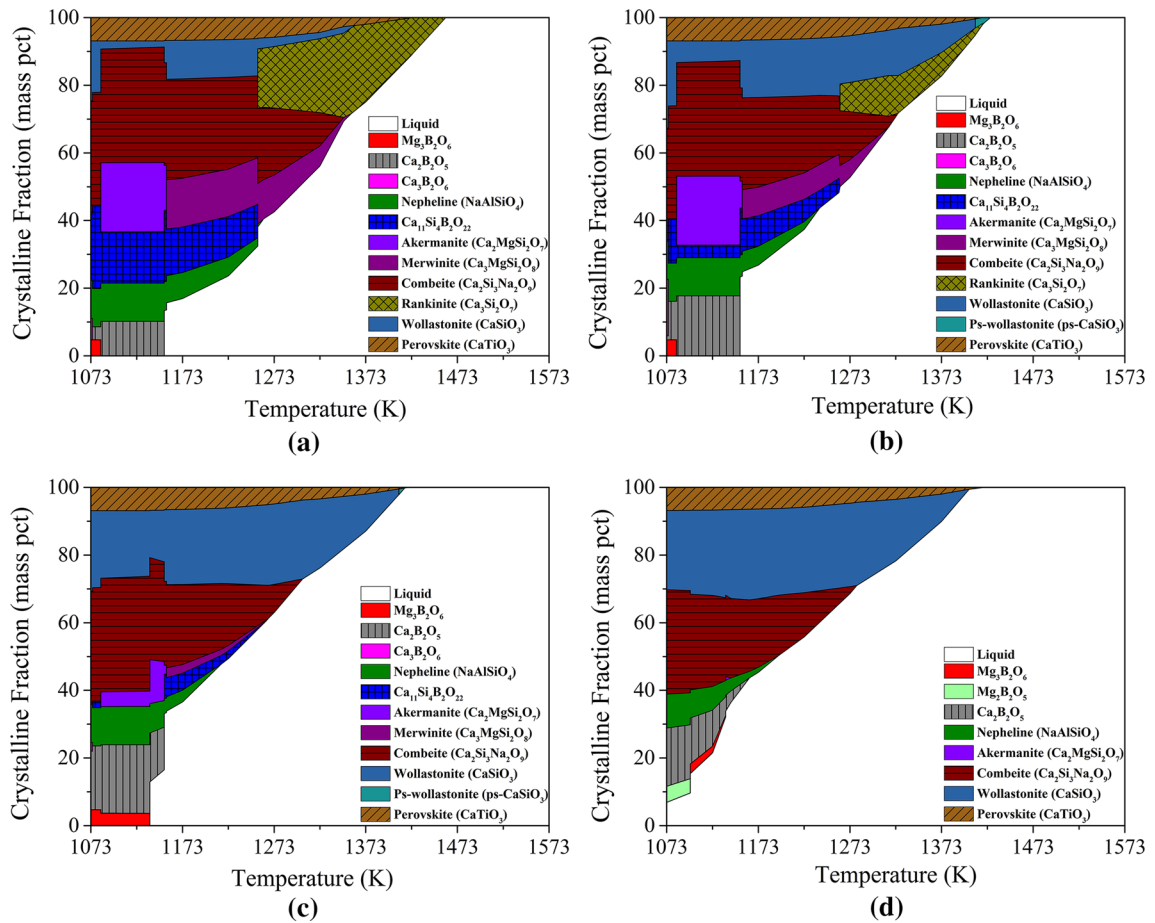


Fig. 13—Crystalline fractions of mold calculated by FactSage 7.0: (a) Sample 1 ( $B_2O_3 = 4.7$  mass pct), (b) Sample 2 ( $B_2O_3 = 6.8$  mass pct), (c) Sample 3 ( $B_2O_3 = 8.6$  mass pct), and (d) Sample 4 ( $B_2O_3 = 10.4$  mass pct).

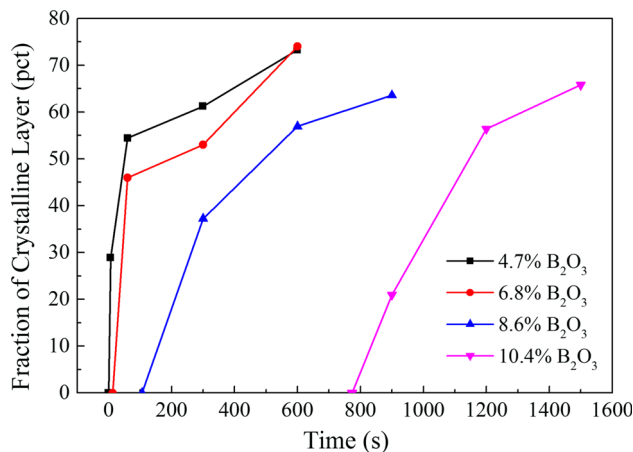


Fig. 14—Crystallinity evolution of mold fluxes in DHTT experiments.

convection flow. It drifted them to the high temperature side where crystals get melted easily, making it difficult to build up a stable crystalline layer adjacent to the liquid mold fluxes. Therefore, the radiative heat transfer

could be less impeded by the loosely bonded crystalline layer near liquid/crystalline interface in Sample 1 than the strongly bonded one near liquid/crystalline interface in Sample 2. The crystal morphology is consistent with that at the liquid/crystalline interface of the flux disk in IET experiments as shown in Figure 16, although the equiaxed crystals in IET samples showed a much larger size than DHTT samples due to a longer growing time. It resulted from the fact that the top surface temperature of the flux disk in IET tests was lower than the high temperature side in DHTT experiments.<sup>[33]</sup> So the equiaxed crystals formed in IET tests could be relatively difficult to melt even if they were drifted to high temperature side. Although the equiaxed crystals showed very high mobility which made the growth of crystalline layer unstable, they were extremely easy to precipitate with a short incubation time. They could act as nucleation sites once they flow into a low temperature zone, promoting the crystallization process of other crystals by lowering thermodynamic barriers. Therefore, it is possible to control the heat transfer rate by designing the ratio of equiaxed crystals to dendritic crystals or other 2D structures. It could be effective to avoid both the high flowability of equiaxed crystals and the relatively long incubation time of dendritic crystals.

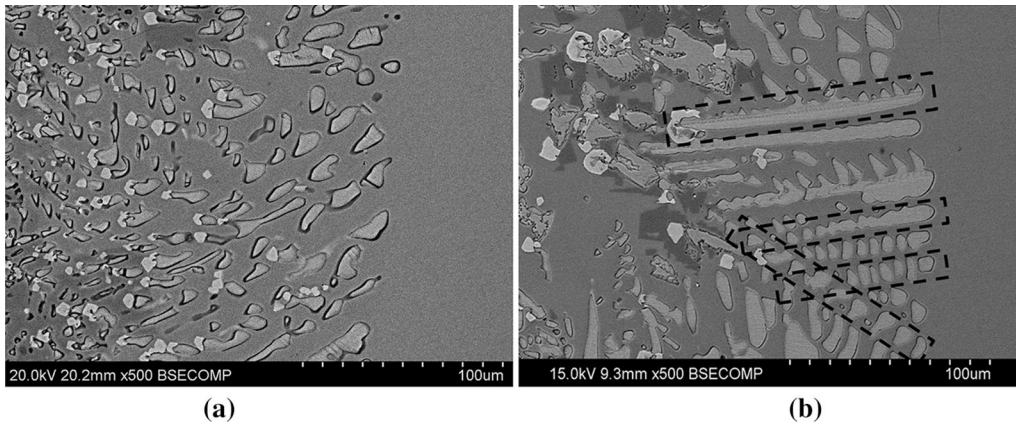


Fig. 15—Microstructure of liquid/crystalline interface of mold flux films in DHTT experiments: (a) Sample 1 ( $B_2O_3 = 4.7$  mass pct), (b) Sample 2 ( $B_2O_3 = 6.8$  mass pct).

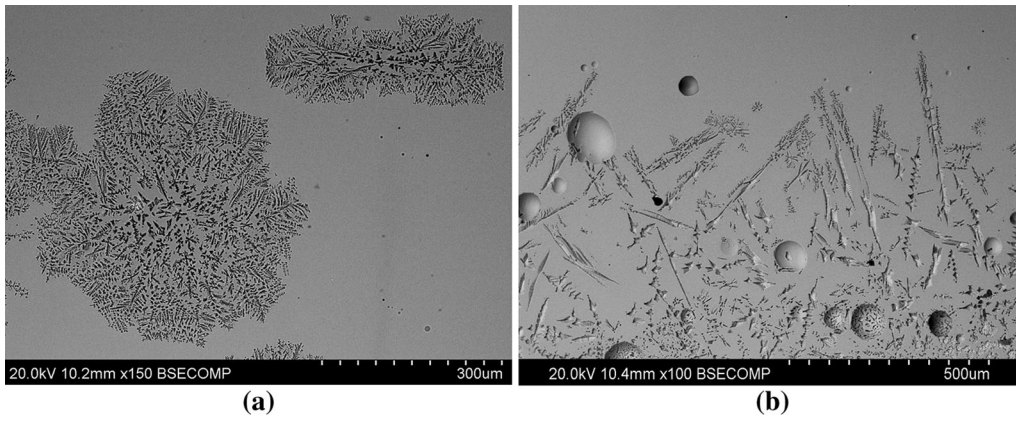


Fig. 16—Microstructure of liquid/crystalline interface of mold flux disk in IET tests: (a) Sample 1 ( $B_2O_3 = 4.7$  mass pct), (b) Sample 2 ( $B_2O_3 = 6.8$  mass pct).

## V. CONCLUSIONS

The crystallization behavior, structure, and heat transfer of fluorine-free mold fluxes with different  $B_2O_3$  content were studied using hot thermocouple technique, Raman spectroscopy, and infrared emitter technique, respectively. The major findings are summarized as follows:

- (1) CCT and TTT diagrams developed using SHTT revealed that the increase of  $B_2O_3$  inhibited the crystallization process of mold fluxes, which was confirmed by DHTT experiments. DHTT experiments also indicated that a three-layer structure—liquid, crystalline, and glass layers—was formed in a thermal field simulating continuous casting mold;
- (2) Major precipitates changed from  $Ca_2MgSi_2O_7$  and  $Ca_{11}Si_4B_2O_{22}$  to  $CaSiO_3$  with the increase of  $B_2O_3$  from 4.7 to 10.4 mass pct as indicated in XRD analysis. Minor precipitates, such as  $Ca_2Si_3Na_2O_9$  and  $CaTiO_3$ , were also detected by XRD. These findings are consistent with thermodynamic calculations carried out using FactSage 7.0;
- (3) The addition of  $B_2O_3$  increased the degree of polymerization by increasing the fraction of  $Q^3$  units and

decreasing the fractions of  $Q^0$  and  $Q^2$  units. The formation of 3D borate structures resulted in a more complex structure of flux melts. However, it was revealed that a dominant role in lowering the crystallinity of fluxes was played by the decrease in the melting temperature with the addition of  $B_2O_3$ ;

- (4) Heat flux measured by IET showed that it reached a minimum value when  $B_2O_3$  content was 6.8 mass pct. Heat flux decreased from 659 to 595  $kW/m^2$  when  $B_2O_3$  content increased from 4.7 to 6.8 mass pct; while a further increase of  $B_2O_3$  concentration from 6.8 to 10.4 mass pct raised the heat flux from 595 to 736  $kW/m^2$ . The increase of crystallinity inhibited the heat transfer which was also influenced by the crystal morphology.

## ACKNOWLEDGMENTS

Financial support by Baosteel through the Baosteel-Australia Joint Research Centre, Abel Metal Services, and Australian Research Council (ARC Linkage Project LP130100773) is gratefully acknowledged.

## REFERENCES

1. A.B. Fox, K.C. Mills, D. Lever, C. Bezerra, C. Valadares, I. Unamuno, J.J. Laraudogoitia, and J. Gisby: *ISIJ Int.*, 2005, vol. 45, pp. 1051–58.
2. A. Grill, K. Sorimachi, and J. Brimacombe: *Metall. Trans. B*, 1976, vol. 7, pp. 177–89.
3. J. Brimacombe and K. Sorimachi: *Metall. Trans. B*, 1977, vol. 8B, pp. 489–505.
4. H. Nakada, M. Susa, Y. Seko, M. Hayashi, and K. Nagata: *ISIJ Int.*, 2008, vol. 48, pp. 446–53.
5. S. Ozawa, M. Susa, T. Goto, R. Endo, and K. Mills: *ISIJ Int.*, 2006, vol. 46, pp. 413–19.
6. A.W. Cramb: *ISIJ Int.*, 2014, vol. 54, pp. 2665–71.
7. M. Susa, A. Kushimoto, R. Endo, and Y. Kobayashi: *ISIJ Int.*, 2011, vol. 51, pp. 1587–96.
8. M. Hayashi, N. Nabeshima, H. Fukuyama, and K. Nagata: *ISIJ Int.*, 2002, vol. 42, pp. 352–58.
9. K.C. Mills: *ISIJ Int.*, 2016, vol. 56, pp. 1–13.
10. G. Wen, S. Sridhar, P. Tang, X. Qi, and Y. Liu: *ISIJ Int.*, 2007, vol. 47, pp. 1117–25.
11. N. Takahira, M. Hanao, and Y. Tsukaguchi: *ISIJ Int.*, 2013, vol. 53, pp. 818–22.
12. H. Nakada and K. Nagata: *ISIJ Int.*, 2006, vol. 46, pp. 441–49.
13. J. Wei, W. Wang, L. Zhou, D. Huang, H. Zhao, and F. Ma: *Metall. Mater. Trans. B*, 2013, vol. 45B, pp. 643–52.
14. L. Zhou, W. Wang, J. Wei, and K. Zhou: *ISIJ Int.*, 2015, vol. 55, pp. 821–29.
15. L. Zhou, W. Wang, and K. Zhou: *ISIJ Int.*, 2015, vol. 55, pp. 1916–24.
16. J. Yang, J. Zhang, Y. Sasaki, O. Ostrovski, C. Zhang, D. Cai, and Y. Kashiwaya: *ISIJ Int.*, 2016, vol. 56, pp. 574–83.
17. J. Yang, J. Zhang, Y. Sasaki, O. Ostrovski, C. Zhang, D. Cai, and Y. Kashiwaya: *Metall. Mater. Trans. B*, 2016, vol. 47B, pp. 2447–58.
18. W. Wang, X. Yan, L. Zhou, S. Xie, and D. Huang: *Metall. Mater. Trans. B*, 2016, vol. 47B, pp. 963–73.
19. J. Fletcher and F. Glasser: *J. Mater. Sci.*, 1993, vol. 28, pp. 2677–86.
20. T. Watanabe, H. Fukuyama, K. Nagata, and M. Susa: *Metall. Mater. Trans. B*, 2000, vol. 31B, pp. 1273–81.
21. X. Qi, G.-H. Wen, and P. Tang: *J. Iron Steel Res. Int.*, 2010, vol. 17, pp. 6–10.
22. J.-Y. Park, G.H. Kim, J.B. Kim, S. Park, and I. Sohn: *Metall. Mater. Trans. B*, 2016, vol. 47B, pp. 2582–94.
23. B. Lu, W. Wang, J. Li, H. Zhao, and D. Huang: *Metall. Mater. Trans. B*, 2013, vol. 44B, pp. 365–77.
24. Y. Sun, J. Liao, K. Zheng, X. Wang, and Z. Zhang: *JOM*, 2014, vol. 66, pp. 2168–75.
25. G.-R. Li, H.-M. Wang, Q.-X. Dai, Y.-T. Zhao, and J.-S. Li: *J. Iron Steel Res. Int.*, 2007, vol. 14, pp. 25–28.
26. L. Zhou, W. Wang, B. Lu, G. Wen, and J. Yang: *Met. Mater. Int.*, 2015, vol. 21, pp. 126–33.
27. L. Zhou, W. Wang, J. Wei, and B. Lu: *ISIJ Int.*, 2013, vol. 53, pp. 665–72.
28. Y. Cui, L. Wang, J. Yang, J. Zhang, Y. Sasaki, and O. Ostrovski: *Steel Res. Int.*, 2015, vol. 86, pp. 662–69.
29. L. Wang, Y. Cui, J. Yang, C. Zhang, D. Cai, J. Zhang, Y. Sasaki, and O. Ostrovski: *Steel Res. Int.*, 2015, vol. 86, pp. 670–77.
30. Y. Kashiwaya, C.E. Cicutti, and A.W. Cramb: *ISIJ Int.*, 1998, vol. 38, pp. 357–65.
31. Y. Kashiwaya, C.E. Cicutti, A.W. Cramb, and K. Ishii: *ISIJ Int.*, 1998, vol. 38, pp. 348–56.
32. B. Ho: Master Thesis, University of Illinois at Urbana-Champaign, 1992.
33. K. Gu, W. Wang, L. Zhou, F. Ma, and D. Huang: *Metall. Mater. Trans. B*, 2012, vol. 43B, pp. 937–45.
34. K. Gu, W. Wang, J. Wei, H. Matsuura, F. Tsukihashi, I. Sohn, and D.J. Min: *Metall. Mater. Trans. B*, 2012, vol. 43B, pp. 1393–1404.
35. Y. Meng and B.G. Thomas: *ISIJ Int.*, 2006, vol. 46, pp. 660–69.
36. Y. Meng and B.G. Thomas: *Metall. Mater. Trans. B*, 2003, vol. 34B, pp. 685–705.
37. A. Yamauchi, K. Sorimachi, T. Sakuraya, and T. Fujii: *ISIJ Int.*, 1993, vol. 33, pp. 140–47.
38. L. Zhou, W. Wang, D. Huang, J. Wei, and J. Li: *Metall. Mater. Trans. B*, 2012, vol. 43B, pp. 925–36.
39. P.E. Ramirez-Lopez, P.D. Lee, K.C. Mills, and B. Santillana: *ISIJ Int.*, 2010, vol. 50, pp. 1797–1804.
40. Y. Sun and Z. Zhang: *Metall. Mater. Trans. B*, 2015, vol. 46, pp. 1549–54.
41. B.O. Mysen and J.D. Frantz: *Am. Mineral.*, 1993, vol. 78, pp. 699–709.
42. Y.-Q. Wu, G.-C. Jiang, J.-L. You, H.-Y. Hou, and H. Chen: *Acta Phys. Sin.*, 2005, vol. 54, pp. 961–66.
43. Y. Kim and K. Morita: *ISIJ Int.*, 2014, vol. 54, pp. 2077–83.
44. R.K. Brow, D.R. Tallant, and G.L. Turner: *J. Am. Ceram. Soc.*, 1996, vol. 79, pp. 2410–16.
45. E.I. Kamitsos, M.A. Karakassides, and G.D. Chryssikos: *J. Phys. Chem.*, 1987, vol. 91, pp. 1073–79.
46. H. Li, Y. Su, L. Li, and D.M. Strachan: *J. Non-Cryst. Solids*, 2001, vol. 292, pp. 167–76.
47. K. Zheng, Z. Zhang, L. Liu, and X. Wang: *Metall. Mater. Trans. B*, 2014, vol. 45B, pp. 1389–97.
48. B.O. Mysen, F.J. Ryerson, and D. Virgo: *Am. Miner.*, 1980, vol. 65, pp. 1150–65.
49. S. Sakka, F. Miyaji, and K. Fukumi: *J. Non-Cryst. Solids*, 1989, vol. 112, pp. 64–68.
50. Z. Wang, Q. Shu, and K. Chou: *ISIJ Int.*, 2011, vol. 51, pp. 1021–27.
51. B.O. Mysen, D. Virgo, and C.M. Scarfe: *Am. Mineral.*, 1980, vol. 65, pp. 690–710.
52. G.H. Kim and I. Sohn: *Metall. Mater. Trans. B*, 2014, vol. 45B, pp. 86–95.
53. I.J. Hidi, G. Melinte, R. Stefan, M. Bindea, and L. Baia: *J. Raman Spectrosc.*, 2013, vol. 44, pp. 1187–94.
54. G. Padmaja and P. Kistaiah: *J. Phys. Chem. A*, 2009, vol. 113, pp. 2397–2404.
55. J. Kline, M. Tangstad, and G. Tranell: *Metall. Mater. Trans. B*, 2015, vol. 46, pp. 62–73.
56. L.-S. Du and J.F. Stebbins: *J. Non-Cryst. Solids*, 2003, vol. 315, pp. 239–55.
57. V.P. Klyuev and B.Z. Pevzner: *Glass Phys. Chem*, 2002, vol. 28, pp. 207–20.
58. J. Yang, Y. Cui, L. Wang, Y. Sasaki, J. Zhang, O. Ostrovski, and Y. Kashiwaya: *Steel Res. Int.*, 2015, vol. 86, pp. 636–43.
59. S.-Y. Choi, D.-H. Lee, D.-W. Shin, S.-Y. Choi, J.-W. Cho, and J.-M. Park: *J. Non-Cryst. Solids*, 2004, vols. 345–346, pp. 157–60.
60. J.E. Shelby: *Introduction to Glass Science and Technology*, 2nd ed., Royal Society of Chemistry, Cambridge, UK, 2005, pp. 11–21.
61. Z. Wang, Q. Shu, and K. Chou: *Steel Res. Int.*, 2013, vol. 84, pp. 766–76.
62. L. Zhou, W. Wang, J. Wei, and B. Lu: *ISIJ Int.*, 2013, vol. 53, pp. 665–72.
63. Q. Shu, Z. Wang, J.L. Klug, K. Chou, and P.R. Scheller: *Steel Res. Int.*, 2013, vol. 84, pp. 1138–45.